Journal of ELECTRONIC MATERIALS, Vol. 50, No. 1, 2021
https://doi.org/10.1007/s11664-020-08560-6


# Melt-Spun SiGe Nano-Alloys: Microstructural Engineering Towards High Thermoelectric Efficiency

AVINASH VISHWAKARMA,[1,2] NAGENDRA S. CHAUHAN ,[3] RUCHI BHARDWAJ,[1,2] KISHOR KUMAR JOHARI,[1,2] SANJAY R. DHAKATE,[1,2] BHASKER GAHTORI,[1,2,5] and SIVAIAH BATHULA [1,2,4,6]

1.—Academy of Scientific and Innovative Research (AcSIR), Ghaziabad, Uttar Pradesh 201002, India. 2.—Division of Advanced Materials and Devices Metrology, CSIR-National Physical Laboratory, Dr. K. S. Krishnan Marg, New Delhi 110012, India. 3.—Micro and Nanofabrication Department, International Iberian Nanotechnology Laboratory, Braga 4715-330, Portugal. 4.—School of Minerals, Metallurgical and Materials Engineering, IIT Bhubaneswar, Bhubaneswar 752050, Odisha, India. 5.—e-mail: bhasker@nplindia.org. 6.—e-mail: sivaiahb@iitbbs.ac.in

Silicon-germanium (SiGe) alloys are prominent high-temperature thermoelectric (TE) materials used as a powering source for deep space applications. In this work, we employed rapid cooling rates for solidification by melt-spinning and rapid heating rates for bulk consolidation employing spark plasma sintering to synthesize high-performance *p*-type SiGe nano-alloys. The current methodology exhibited a TE figure-of-merit ($ZT$) $\approx$ 0.94 at 1123 K for a higher cooling rate of $\sim 3.0 \times 10^7$ K/s. This corresponds to $\approx$ 88% enhancement in $ZT$ when compared with currently used radioisotope thermoelectric generators (RTGs) in space flight missions, $\approx$ 45% higher than pressure-sintered *p*-type alloys, which results in a higher output power density, and TE conversion efficiency ($\eta$) $\approx$ 8% of synthesized SiGe nano-alloys estimated using a cumulative temperature dependence (CTD) model. The $ZT$ enhancement is driven by selective scattering of phonons rather than of charge carriers by the high density of grain boundaries with random orientations and induced lattice-scale defects, resulting in a substantial reduction of lattice thermal conductivity and high power factor. The TE characteristics of synthesized alloys presented using the constant property model (CPM) and CTD model display their high TE performance in high-temperature regimes along with wide suitability of segmentation with different mid-temperature TE materials.

(Received June 11, 2020; accepted October 9, 2020; published online November 2, 2020)

**Graphic Abstract**

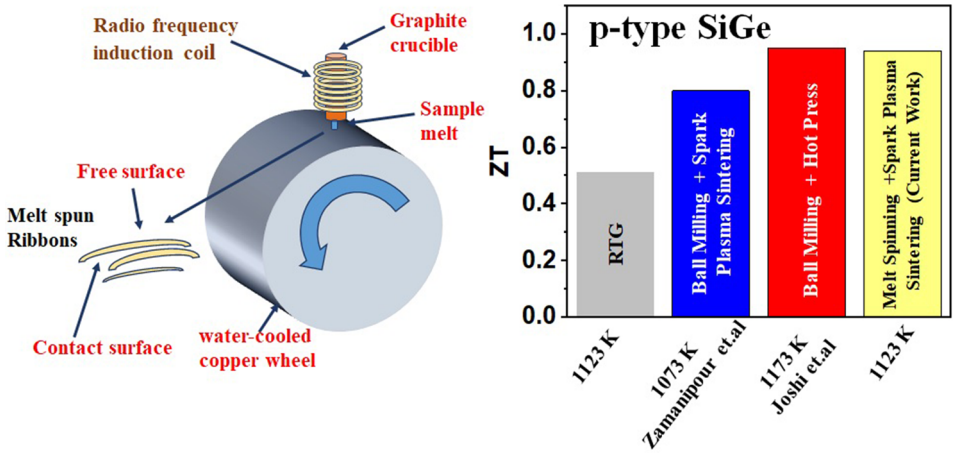


**Key words:** SiGe alloys, lattice thermal conductivity, melt-spun, rapid solidification, spark plasma sintering

## INTRODUCTION

Thermoelectric (TE) technology has a long history of providing simple and reliable power generation solutions for increasing the energy efficiency of various industrial processes and providing power in remote applications (space probes, space stations). The success of radioisotope thermoelectric generators (RTGs) as safe, reliable, long-lived power systems in space exploration missions had motivated the future expansion of TE technology in terrestrial applications, specifically in the areas of waste heat recovery, energy harvesting, and auxiliary power units.[1] At present, TE materials are widely explored as a waste heat recovery system in automotive exhaust and industrial processes, all of which generate an enormous amount of unused waste heat. However, the conversion efficiency of a TE device depends on the figure of merit ($ZT$), which is a material's property and can be represented as $ZT = \left(\frac{S^2\sigma}{\kappa}\right)T$, wherein at absolute temperature (T), $S$ and $\sigma$ represent the Seebeck coefficient and electrical conductivity, respectively, while the total thermal conductivity ($\kappa$) is derived from electronic ($\kappa_e$) and lattice ($\kappa_L$) contributions ($\kappa = \kappa_e + \kappa_L$). To achieve high efficiency in TE devices, materials with high $ZT$ are desired. The challenge in TE research is to incorporate all the desirable features associated with the charge and thermal transport altogether in a single material.[2]

Amongst actively explored TE materials for high-temperature application,[3–7] SiGe-based alloys are most promising, particularly in higher-temperature regimes greater than 973 K, owing to their high mechanical strength and high-temperature thermal stability, as established by thermal cycling studies indicating minimal degradation in TE properties up to 1273 K.[3,8] To date, several nanostructuring approaches have been employed to enhance the $ZT$ of various TE materials.[2,9] In $p$-type SiGe alloy, the existing RTGs[2] used for space applications are operational at $ZT \approx 0.50$ at 1123 K; further consolidation by hot-pressed technique exhibited a $ZT \approx 0.65$.[10,11] On applying nanostructuring through the ball-milling technique followed by hot-pressing, an improvement in $ZT \approx 0.95$ was attained due to the formation of nanostructures,[12] resulting in lower thermal conductivity. Furthermore, ball-milled nanostructured powders of $p$-type SiGe alloy consolidated by employing rapid sintering significantly enhanced the $ZT \approx 1.2$ at 1173 K.[3] Similarly, high $ZT \approx 1.5$ at 1173 K was attained in an $n$-type counterpart with a similar methodology, which established the efficacy of bulk nanostructured alloys for TE applications.[13] However, the ball-milling process is often time-consuming (60–90 h) and adds to the material processing costs. Moreover, in the case of SiGe alloys, there is an inherent risk of contamination of SiGe particles with the milling medium and also chances of nano-inclusion oxidation (i.e. formation of $SiO_2$) during the long hours of the process, which may deteriorate the nanostructuring effect on TE properties. In the melt-spun process, to avoid contamination, ceramic crucibles are generally used to melt these alloys under vacuum/inert gas. Subsequently, splat cooling of the process is sufficient enough to obtain the nanocrystalline microstructure in short time in comparison to ball milling.

In this context, rapid solidification by high cooling rates attained via the melt-spun technique for synthesizing nano-ribbons and their bulk consolidation is an advanced processing approach for the fabrication of homogeneous alloy, which has been explored in recent years for synthesizing different kinds of state-of-the-art TE materials, such as $Bi_2Te_3$ and its alloys,[14–21] SnTe,[22–25] skutterudites,[26–29] half-Heusler,[30–32] silicides,[33–36] $Zn_4Sb_3$,[37] $AgSbTe_2$,[38] and GeTe.[39,40]. The melt-spun synthesis route enables the formation of extremely ultrafine grains with greater solid solubility and a tendency for nucleation of many metastable crystalline phases with a considerable grain boundary area. Simultaneously, rapid cooling rates in the order of $10^6$–$10^7$ K/s and processing of large volumes of materials with refined microstructure and improved chemical homogeneity are possible with melt-spinning.[41,42] Recently, we employed the rapid solidification by melt-spun technique followed by spark plasma sintering (MS-SPS) for *n*-type SiGe nanostructured alloys to realize *ZT* around unity. The *ZT* enhancement was mainly attributed to a severe reduction in $\kappa$, resulting from the huge amorphous grain boundary area and nanostructured microstructure.[43]

In the current study, we have implemented MS-SPS methodology to synthesize *p*-type SiGe alloys with high TE performance and comparable *ZT* as its *n*-type counterparts. The arc-melted ingots were melt-spun to obtain the nano-ribbons at varying wheel speed to realize complex micromorphology consisting of an amorphous phase near the direct contact side of the wheel and very fine nano-sized grain at the free side of the copper wheel.[14] Subsequently, these nano-ribbons were consolidated by employing SPS at rapid heating rates to retain nano-scale features with minimal growth. The nano-grained microstructure resulting from MS-SPS methodology brings about a sufficiently reduced thermal conductivity owing to stronger phonon scattering compared to the charge carrier scattering. The implication of varying cooling rates on TE transport properties by the MS-SPS approach was presented and corroborated with the detailed microstructural investigation. Additionally, the TE device performance parameters were theoretically estimated using the cumulative temperature dependence (CTD) model and constant property model (CPM) for comparison to provide future direction towards designing high-performance TE devices in high-temperature regimes.

## EXPERIMENTAL DETAILS

The nanostructured *p*-type SiGe alloy was prepared using high-purity elemental powder of silicon (99.98%), germanium (99.99%), and 1.2% of B powder (>99%, Alfa Aesar) in the stoichiometric proportion of $Si_{80}Ge_{20}$, which was arc-melted (MAM-1, Edmund Bühler GmbH, Germany) multiple times in an argon gas atmosphere to obtain a homogeneous mixture in the form of ingots. Subsequently, the arc-melted ingots were loaded into a melt-spun graphite crucible (M/s. Edmund Bühler GmbH, Germany), and they were inductively melted at an optimal temperature of 1550 °C under a vacuum of $10^{-6}$ mbar. Afterward, the liquid melt was ejected at a distance of 0.4 mm from nozzle to wheel, on to a fast-rotating water-cooled copper wheel (dia. 250 mm) at various wheel speeds, i.e. 23 m/s, 27 m/s, and 31 m/s, which was selected based on the available literature data of melt-spinning of various TE materials.[14–40] The obtained melt-spun ribbons were further ground into fine powders before sintering. Graphite die of diameter 12.7 mm was used for bulk consolidation and rapid sintering employing spark plasma sintering (SPS-725, M/s. Fuji Electric, Japan) at 1150°C under a uniaxial pressure of 60 MPa and withholding time of 3 min under vacuum of ~10 Pa.

The x-ray powder diffractometer (Miniflex-II, M/s. Rigaku Corporation, Japan) with Cu $K_\alpha$ ($\lambda_0$ = 1.5406 Å) was used for phase identification of the synthesized samples. Subsequently, morphological studies were carried out using a field emission scanning electron microscope (FESEM, Supra 40VP, M/s. Zeiss, UK). Furthermore, selected-area electron diffraction patterns (SAEDP) and lattice-scale micrographs were recorded by a high-resolution transmission electron microscope (HR-TEM, FEI, G2 F30 STWIN) to confirm the defects and grain orientation.

Firstly, thermal diffusivity was measured under a vacuum of $10^{-3}$ mbar using a laser flash system (LFA 1000, M/s. Linseis, Germany) with a sample of diameter 12.7 mm having a thickness of 2.5 mm. Simultaneously, $C_p$ was measured using differential scanning calorimetry (DSC, 404 F3, M/S Netzsch, Germany), and $\rho$ was measured (Mettler Toledo, model: ML204 /A01) based on the Archimedes principle. Afterward, electrical conductivity and Seebeck coefficient were measured using the four-probe method (ZEM-3, M/s. Ulvac Inc., Japan) in a helium atmosphere, on rectangular specimens 12 mm long × 4 mm wide × 2 mm thick. To understand electrical transport properties, the room-temperature charge carrier mobility and concentration were measured employing a Hall effect measurement system (HEMS, M/s Nano-magnetics, UK). The uncertainties evaluated in transport measurement are ± 6% for $D$, ± 7% for $\sigma$, ± 7% for $S$, ± 10% for $C_p$, and ± 0.5% for $\rho$.

## RESULTS AND DISCUSSION

The MS-SPS methodology for microstructural engineering at different cooling rates was examined through varying wheel speeds, whose microstructural and thermoelectric characterization is presented in subsequent sections. The average cooling rate ($dT/dt$) was determined using the formula:[34,44]

$$\frac{dT}{dt} = h * (T_h - T_w)/C_p * d * t \quad (1)$$

where $h$ = heat transfer coefficient, $t$ = thickness of the ribbon, $C_p$ = heat capacity of the material, $d$ = density, $T_w$ = temperature of the water-cooled wheel, and $T_h$ = hot-end temperature of the melted material. During the processing of all samples, other parameters such as injection pressure, the distance from nozzle to wheel, and slit width were kept constant. The average cooling rate holds direct dependence with wheel speed and was carried out at $9.7 \times 10^6$ K/s (23 m/s), $1.5 \times 10^7$K/s (27 m/s), and $3.0 \times 10^7$ K/s (31 m/s). The maximum wheel speed of the water-cooled copper wheel for melt-spinning was 31 m/s, due to equipment limitations.

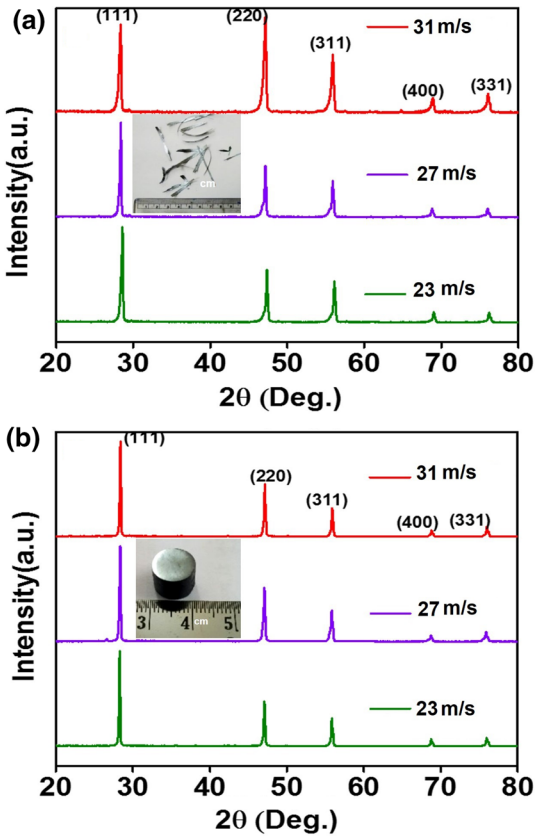


Fig. 1. XRD patterns of *p*-type SiGe nano-alloys synthesized at various wheel speeds: (a) MS ribbons (inset: MS ribbons with centimeter scale) and (b) MS-SPS samples (inset: MS-SPS pellet with centimeter scale).

## Phase Composition and Microstructural Analysis

The measured XRD patterns of the as-synthesized *p*-type SiGe melt-spun ribbons and MS-SPS pellet samples synthesized at the different wheel speeds are presented in Fig. 1a and b, respectively. The measured XRD pattern is well-indexed with peaks of Si for all wheel speeds, suggesting the complete solid solubility of Ge in Si and pure phase formation of *p*-type $Si_{80}Ge_{20}$ alloy having a diamond-like cubic structure (space group: 227, Fd $\bar{3}$ m), similar to previous reports on *p*-type SiGe nano-alloys.[3] As evident from Fig. 1a, the relatively high intensity of the peak corresponding to (220) plane indicates the preferred orientation of the melt-spun ribbon during rapid solidification, as observed previously.[45–47] This may be ascribed to the crystallization and growth of a larger number of crystals along the preferred direction during the melt-spun process. However, during grinding of melt-spun ribbons into powders and subsequent sintering, the preferential ordering was disrupted, resulting in polycrystalline grains.[48]

The average crystallite size of MS ribbons and MS-SPS samples were quantitatively assessed using XRD data employing the Williamson–Hall method, as shown in Table I. The broadened peaks for the MS ribbons (Fig. 1a), as compared to MS-SPS samples (Fig. 1b), indicates significant grain growth during sintering, as presented in Table I, which shows an increased crystallite size of MS-SPS samples (39–46 nm) in comparison to MS ribbons (19–30 nm) having thickness ≈ 15–25 $\mu$m. The average crystallite size indicates independence of synthesized MS ribbon characteristics with respect to cooling time, i.e. wheel speed, which is primarily due to difficulty in controlling the growth kinetics during melt-spinning despite similar conditions during synthesis. However, the result indicates that

**Table I. Melt-spinning parameters and Hall measurement data of spark plasma-sintered *p*-type $Si_{80}Ge_{20}$ nano-alloys synthesized at different wheel speeds ($dT/dt$ = cooling rate; $p$ = carrier concentration; $\mu$ = mobility; $m^*$ = effective mass; MS: melt-spun; SPS: spark plasma sintering)**

| Wheel speed (m/s) | Thickness of ribbons ($\mu$m) | $dT/dt$ (K/s) | Average crystallite size (nm) | | $p \times 10^{19}$ ($cm^{-3}$) | $\mu$ ($cm^2$/V s) | $m^*$ |
|---|---|---|---|---|---|---|---|
| | | | MS | MS-SPS | | | |
| 23 | 25 | $9.7 \times 10^6$ | 27 | 43 | 24.2 | 23.8 | 1.79 $m_e$ |
| 27 | 21 | $1.5 \times 10^7$ | 30 | 46 | 9.3 | 34.5 | 1.72 $m_e$ |
| 31 | 15 | $3.0 \times 10^7$ | 19 | 39 | 64.2 | 22.5 | 2.56 $m_e$ |

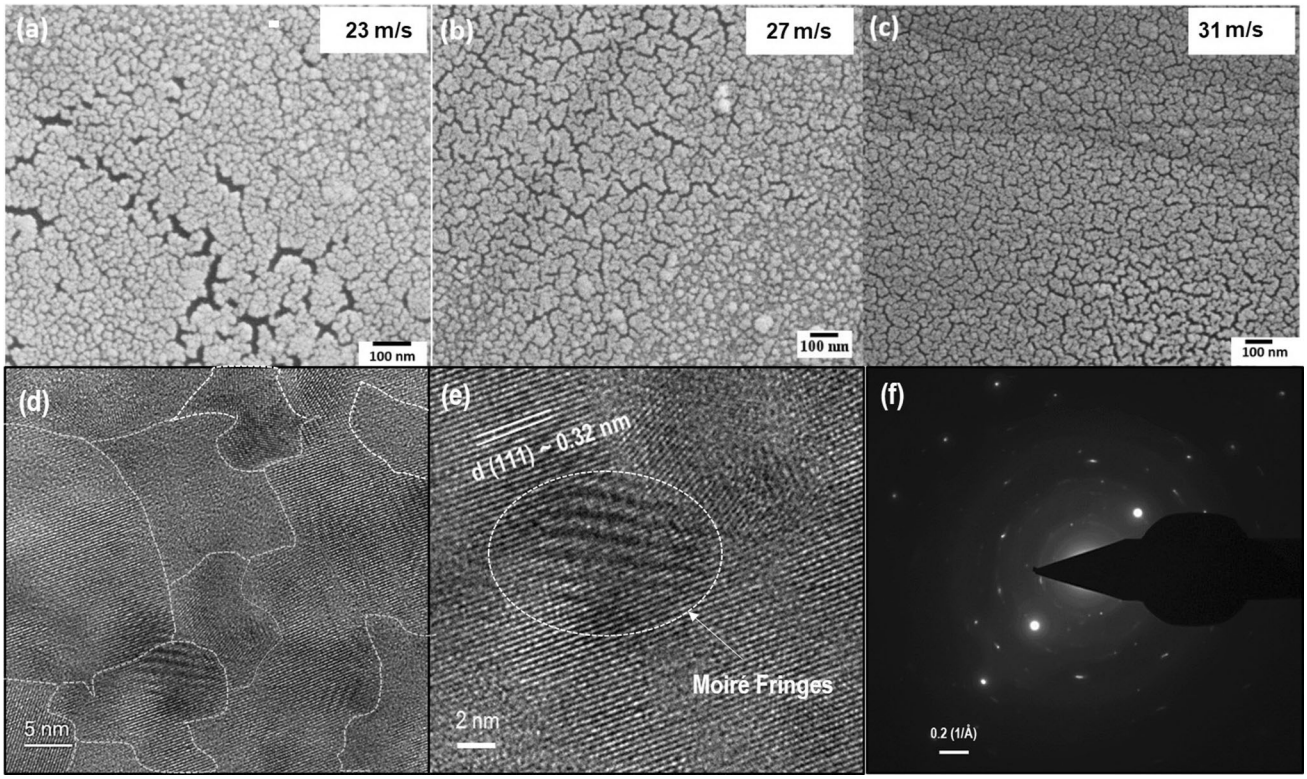


Fig. 2. FE-SEM microstructures of the synthesized MS-SPS samples of *p*-type $Si_{80}Ge_{20}$ nano-alloys at various wheel speeds: (a) 23 m $s^{-1}$ (b) 27 m $s^{-1}$, and (c) 31 m $s^{-1}$. HR-TEM images of MS sample of *p*-type SiGe alloy: (d) ultrafine distribution of grains with different orientations, (e) lattice-scale image of SiGe nano-alloys consisting of lattice-scale defects, and its corresponding (f) selected-area diffraction pattern.

higher cooling rates resulting from higher wheel speed result in reduced crystallite size. The optimal sintering condition yields the sintered product with a near-theoretical density.

The microstructural features of the representative MS-SPS samples at different wheel speeds were examined by FE-SEM and shown in Fig. 2a–c. The nano-grained microstructure for all the wheel speeds is consistent with the XRD analysis. Further, varying wheel speeds and other process parameters significantly affected the physical characteristics and microstructure of ribbons, which is quite similar to other state-of-the-art TE materials synthesized by melt-spinning technique.[14–40] Despite observed grain growth, the nanostructures were retained in the samples during sintering due to the application of high heating rates for grain refinement, similar to the observation made in higher manganese silicides.[34] It is worth emphasizing that the grain growth kinetics and densification during sintering were dependent on the MS ribbon characteristics, as shown in Table I, wherein changes observed in microstructural, electrical, and thermal parameters of MS-SPS samples are following the melt-spun ribbon characteristics, as observed previously.[42,49]

Furthermore, the microstructural features were examined using HR-TEM. As shown in Fig. 2d, the lattice-scale image of the representative MS SiGe nano-alloy at higher wheel speed (31 m/s) indicates a nano-crystallite with random orientation in the microstructure. The lattice-scale image shown in Fig. 2e displays the presence of Moiré fringes due to overlapping of nano-crystallites and the high density of dislocations region marked. Furthermore, the selected area electron diffraction pattern (SAEDP) of nano-grains corresponding to Fig. 2e is presented in Fig. 2f, which shows planes in reciprocal space corresponding to the cubic crystal structure of Si and nanostructure nature of grains. The observed planes are in close agreement with those obtained in the XRD pattern.

## Electrical Transport Measurements

The temperature-dependent $\sigma$ of MS-SPS *p*-type SiGe nanostructured alloy at different wheel speeds is shown in Fig. 3a and also compared with the data of RTGs[2] of similar alloy composition, which are currently being used in deep space applications. For all the samples, $\sigma$ decreased with increasing temperature, indicative of degenerate semiconducting behavior. To better illustrate the electrical conduction, the Hall measurement was carried out to determine the charge carrier concentration ($p$) and carrier mobility ($\mu$), and is presented in Table I. The measured $p$ and $\mu$ values are comparable to previous reports on similar composition.[11,16,42,50,51] At room temperature, the highest $\sigma \approx 24.4 \times 10^4$ S $m^{-1}$ was observed for the sample synthesized at 31 m/s as a

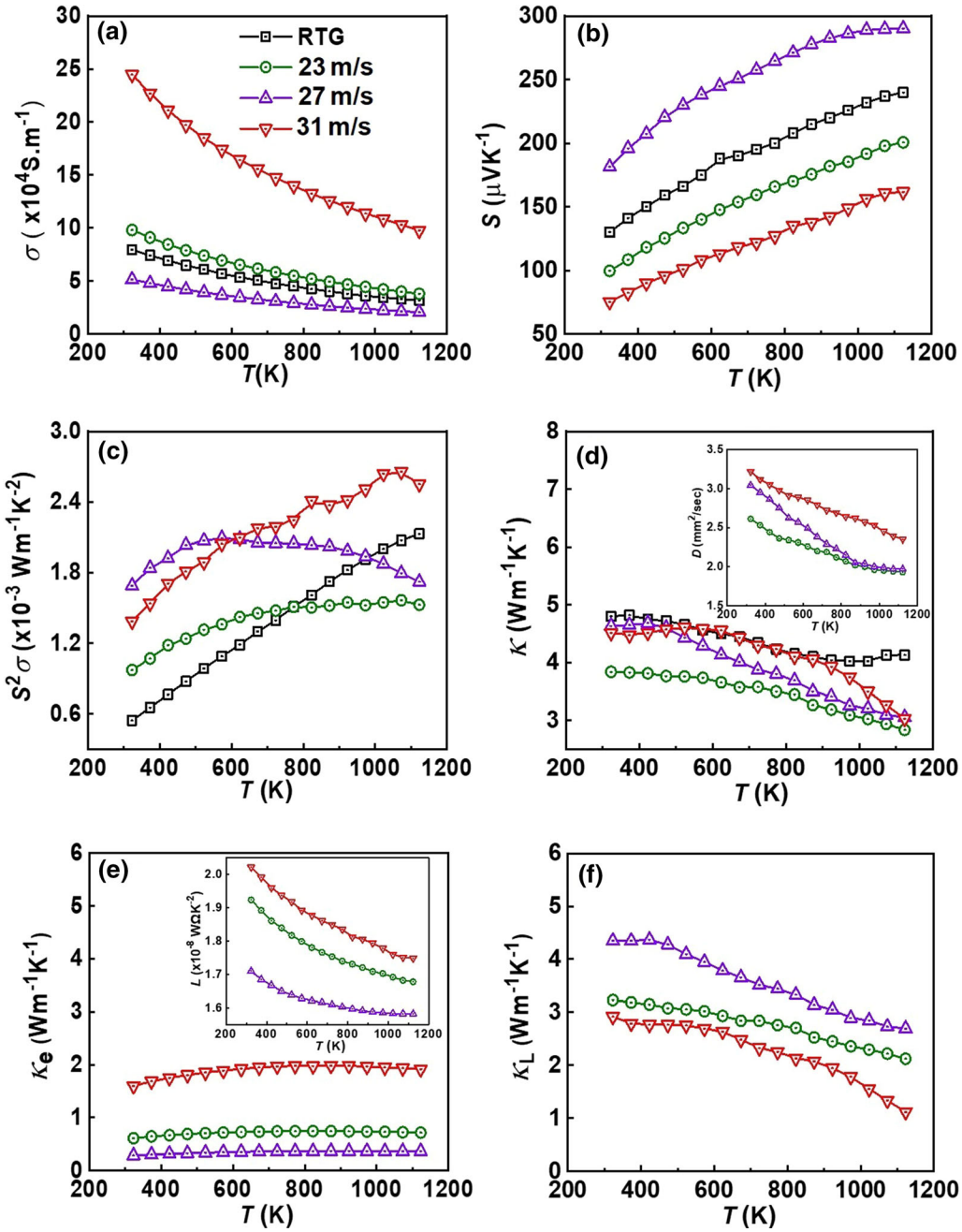


Fig. 3. Thermoelectric transport properties of SiGe *p*-type nano-alloys at different wheel speeds: (a) electrical conductivity, (b) Seebeck coefficient, (c) power factor, (d) total thermal conductivity (inset: thermal diffusivity), (e) electrical thermal conductivity (inset: Lorenz number), and (f) lattice thermal conductivity.

result of its high $p$, which may be attributed to limited precipitation of diffused boron atoms as compared to other samples due to higher cooling rate, thus enhancing the concentration of ionized boron acceptors in the lattice.[52] Similarly, the lowest $\sigma \approx 5.1 \times 10^4$ S m$^{-1}$ was observed for the sample synthesized at 27 m/s, which exhibits the lowest $p$. Interestingly, the sample synthesized at 27 m/s also exhibited the highest $\mu$ (Table I) amongst all samples, which can be ascribed to its larger crystallite size. It is noteworthy that $\sigma$ of the synthesized nano-alloys was higher than nanostructured *p*-type SiGe alloys synthesized by HEBM-SPS[3] and RTGs,[2] which may be attributed to higher carrier concentration, indicating better solubility of diffused boron atoms by rapid cooling and sintering during MS-SPS.[52,53] Moreover, the $\mu$ showed a direct dependence with crystallite size and was found to be minimum, i.e. 22.5 cm$^2$/Vs at higher wheel speed (31 m/s) with the lowest crystallite size ($\sim$39 nm). The lower $\mu$ of the charge carriers is mainly due to the presence of excessive grain

boundaries, which are acting as charge traps and detrimental to $\sigma$ due to charge-charge carrier scattering.

The Seebeck coefficient ($S$) of MS-SPS samples with respect to temperature is shown in Fig. 3b, which is positive for all samples, indicating holes as majority carriers with $p$-type conduction. The measured $S$ indicates strong coupling with an inverse relation to the $\sigma$. The carrier effective mass ($m^*$) was estimated approximately using the Pisarenko relationship between $S$ and $p$, which is expressed using Mott's formula (valid for metals or degenerate semiconductors[54,55]): $S = \left(8\pi^2 k_B^2/3eh^2\right) m^* T(\pi/3p)^{\frac{2}{3}}$, wherein $p$, $k_B$, and $h$ are carrier concentration, Boltzmann constant, and Planck constant, respectively. The $m^*$, as shown in Table I, lies in a similar range as observed previously,[50] particularly for lower wheel speeds. Surprisingly, $m^* \approx 2.56\ m_e$ is maximum for higher wheel speeds (31 m/s), which although consistent with its lower $\mu$, surprisingly did not result in higher $S$, as observed in Fig. 3b. This can be explained by higher $n$, which tends to subdue the gain of higher $m^*$ on $S$, resulting in lowered $S$.

Figure 3c displays the power factor (PF) of the synthesized MS-SPS samples, which on average increases with increasing wheel speed and is considerably higher than RTGs,[2] especially in lower temperatures (<773 K). This is mainly an outcome of optimal carrier characteristics in all the MS-SPS samples, which is directly correlated to precipitation of diffused boron atoms due to a higher cooling rate, thus enhancing the concentration of ionized boron acceptors in the lattice due to splat cooling. Thus, lower sizes of crystallites with a higher density of boundaries and interfaces in MS-SPS samples along with greater solubility are favorable for attaining higher PF in SiGe-based alloys.[16,42,52,53]

## Thermal Transport Measurements

Thermal conductivity of all synthesized samples were calculated using the equation $\kappa = D \times \rho \times C_p$, where $D$ = thermal diffusivity, $\rho$ = density, and $C_p$ = specific heat. The temperature-dependent total thermal conductivity ($\kappa$) of MS-SPS samples is shown in Fig. 3d, which decreases with increasing temperature for all samples. The obtained $\kappa$ for MS-SPS $p$-type $Si_{80}Ge_{20}$ nano-alloys were substantially lower than RTGs, due to enhanced phonon scattering mostly by grain boundary scattering. As shown in Fig. 3d, $\kappa$ obtained by nanostructuring employing MS-SPS is much lower than RTGs, which is mainly due to the large reduction in grain size as compared to bulk RTGs,[8] thus establishing it as an efficient nanostructuring route to decrease the $\kappa_L$ in similar SiGe alloys. The $D$ of the synthesized alloys is shown in the inset of Fig. 3d, and measured $C_p$ varies in the range of 0.4–0.6 $Jg^{-1}\,K^{-1}$ in the measured temperature regime.

To better elucidate the thermal transport, lattice ($\kappa_L$) and electronic ($\kappa_e$) contribution to total $\kappa$ was evaluated. The $\kappa_e$ shown in Fig. 3e was estimated using Wiedemann–Franz law as $\kappa_e = L\sigma T$, where $L$ = the Seebeck-dependent Lorenz number given by $L = \left[1.5 + \exp\left[-\frac{|S|}{116}\right]\right] \times 10^{-8}\ W\Omega K^{-2}$ where $S$ represents the experimentally measured Seebeck coefficient in $\mu$V/K.[56–58] The estimated $L$ lies in the range of 1.6–2.05 $\times\ 10^{-8}\ W\Omega K^{-2}$ and is shown in the inset of Fig. 3e. The $\kappa_e$ attained was maximum for the higher wheel speed (31 m/s) sample, which explains its relatively higher $\kappa$ and can be ascribed to its high $\sigma$ in comparison to other samples. The $\kappa_L$, which mainly depends upon lattice vibrations and microstructural features, was evaluated by subtracting $\kappa_e$ from $\kappa$ ($\kappa_L = \kappa - \kappa_e$) and is shown in Fig. 3f. The $\kappa_L$ decreases with increasing temperature and is primarily attributed to an extensive grain boundary scattering by the random orientation of nano-grains. The lowest $\kappa_L$ ($\approx 0.9\ Wm^{-1}\,K^{-1}$) was obtained for the higher wheel speed (i.e. 31 m/s) sample, which also shows the lowest average crystallite size (Table I). Also, the strain fields and high-angle grain boundaries of nanostructured microstructures introduced by the MS process (Fig. 2) led to favorable grain refinement, which particularly targets low-frequency phonons and is responsible for $\kappa_L$ reduction near lower-temperatures ranges, as observed in previously reported studies in melt-spun TE materials.[14–40]

At higher temperatures, the reduction in $\kappa_L$ of the synthesized alloys becomes more prominent, which can be primarily attributed to scattering high-frequency phonons by point defects and Umklapp processes.[59] The reduction in $\kappa_L$ is higher for higher wheel speed and can be explained using kinetics of temperature-dependent precipitation and solubility of boron. Previously, theoretical calculations for $Si_{0.8}Ge_{0.2}$ suggested an increase of boron precipitation due to nanostructuring, resulting in higher thermal instability of nanostructured $Si_{0.8}Ge_{0.2}$.[53] Thus, a higher cooling rate corresponding to lower crystallite size is anticipated to be more thermally unstable, which is corroborated by thermal transport measurements. Moreover, the reversible nature of boron precipitation in $Si_{0.8}Ge_{0.2}$ alloys observed previously during high-temperature annealing[60] is expected to suppress bipolar conduction at high temperatures, as observed in all the synthesized melt-spun nanostructured alloy at higher temperatures. The increased solid solubility of boron by its re-dissolution is more significant at a temperature greater than the temperature at which boron precipitation occurs (i.e. above 873 K), which is apparent in Fig. 3f.

## Compatibility Factor

The concept of segmentation has been proposed in the literature for achieving higher efficiency, in which different materials of high efficiency were segmented according to their temperature range.[61]

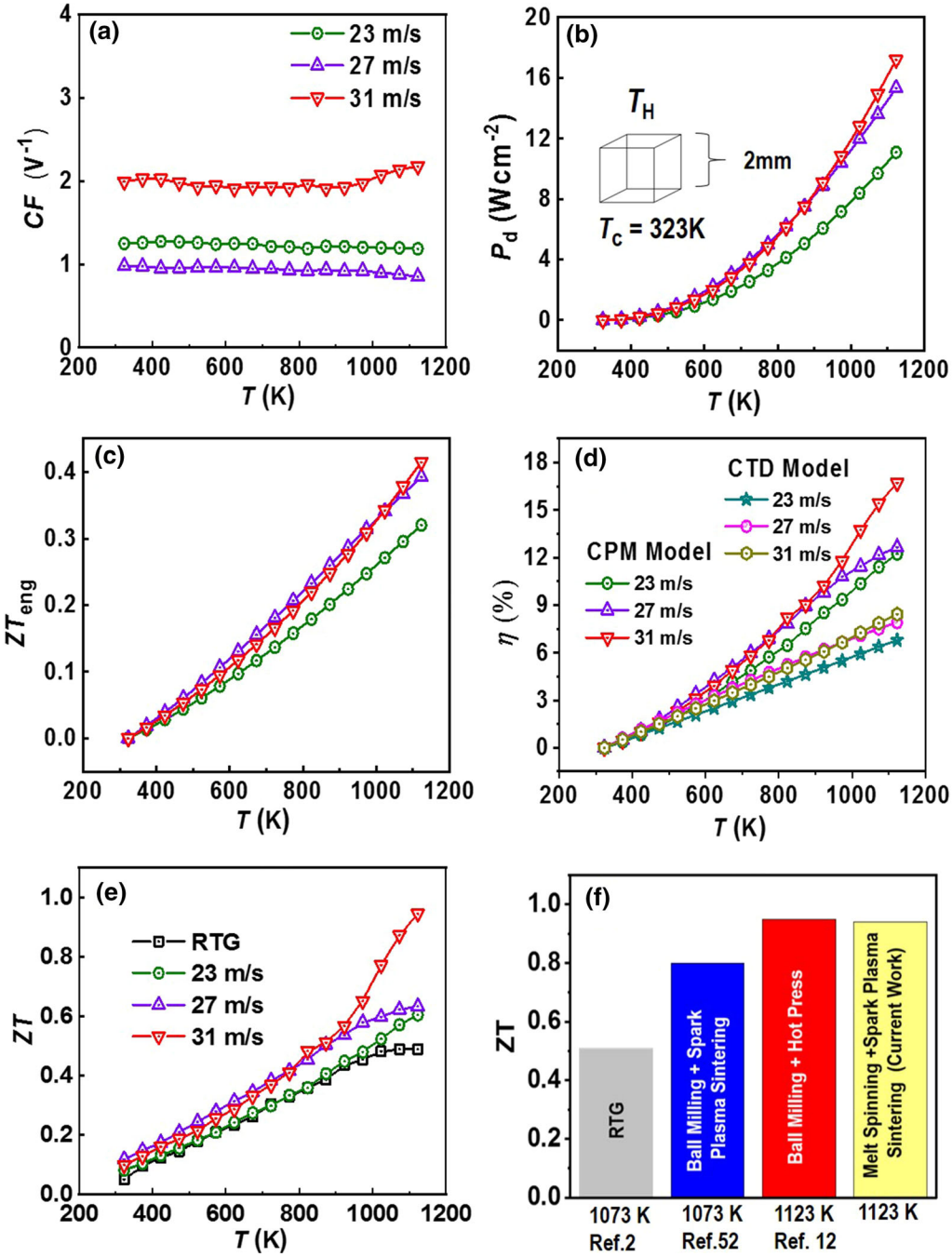


Fig. 4. Theoretically estimated TE device parameters of SiGe *p*-type nano-alloys: (a) thermoelectric compatibility factor (*CF*); (b) output power density ($P_d$); (c) engineering *ZT* ($ZT_{eng}$); (d) thermoelectric efficiency ($\eta$); (e) *ZT*; and (f) comparison of *ZT* with the previous reports[2,12,52] of similar alloy composition.

The compatibility factor (*CF*) is the parameter by which the efficiency of segmentation is calculated. Materials with a difference in *CF* less than 2 can be used for segmentation with other TE materials. The *CF* is estimated[61] as $CF = \frac{\sqrt{1+ZT}-1}{ST}$, and is shown in Fig. 4a for the synthesized MS-SPS samples. The *CF* obtained is invariable with increasing temperature, and it is akin to the various other established *p*-type TE materials such as half-Heusler, SnTe, PbTe, $CeFe_4Sb_{12}$, and TAGS.[61–64] Hence, to achieve highly efficient TE devices for power generation, *p*-type SiGe nano-alloy synthesized through the MS-SPS methodology would be a worthy candidate for segmentation with other state-of-the-art TE materials.[65–67]

## Thermoelectric Performance

The output power density, which depends on dimensions of both the TE legs and the material

properties, was estimated by considering $T_C$ = 323 K and leg length ($L$) = 2 mm, with the assumption of a cubic-shaped TE leg as shown in the inset of Fig. 4b. The $P_d$ at $\eta_{max}$ is evaluated through the CTD model:[43,68]

$$P_d = \frac{(PF)_{eng}(T_H - T_C)^2}{4L} \quad (2)$$

where $PF_{eng}$ is the engineering power factor, T~$T_H$ = hot-side temperature, and $T_C$ = cold-side temperature. The $ZT_{eng}$, as the steady indicator and linear display correlation to $\eta_{max}$ as shown in Fig. 4c, was estimated as expressed below:[69,70]

$$ZT_{eng} = Z_{eng}\Delta T = \frac{\left(\frac{1}{\Delta T}\int_{T_C}^{T_H} S(T_H)dT\right)^2}{\frac{1}{\Delta T}\int_{T_C}^{T_H}\rho(T_H)dT * \frac{1}{\Delta T}\int_{T_C}^{T_H}\kappa(T_H)dT}\Delta T = \frac{PF_{eng}}{\frac{1}{\Delta T}\int_{T_C}^{T_H}\kappa(T_H)dT}\Delta T \quad (3)$$

where $Z_{eng}$ = engineering $ZT$, $K^{-1}$, $PF_{eng}$ = engineering power factor, $Wm^{-1}$ $K^{-2}$. The higher power factor (Fig. 3c), which is also substantiated by high $(PF)_{eng}$ shown in Fig. 4c, explains the higher output power density observed in all melt-spun alloys. Usually, the TE conversion efficiency is estimated by a conventionally used analytical model, i.e. CPM,[71] which assumes constant physical properties with respect to temperature. The maximum efficiency using the CPM is estimated as

$$\eta_{max} = \frac{\Delta T}{T_H}\frac{\sqrt{1+ZT_{avg}}-1}{\sqrt{1+ZT_{avg}}+\frac{T_C}{T_H}} \quad (4)$$

where T~$T_H$ = hot-side temperature and $T_C$ = cold-side temperature of a TE material. Using the CPM considering the temperature boundary condition at $T_C$ = 323 K, the predicted maximum efficiency was obtained ($\eta \sim 16\%$) for higher wheel speed (31 m/s), as shown in Fig. 4d. However, these estimations are temperature-independent and often overestimate or underestimate a material's efficiency, which misleads the design processing of TE module devices.

Subsequently, for predicting the practical performance of the synthesized TE materials more accurately, the cumulative temperature dependence of TE transport properties is taken into account using an analytical CTD model.[69,70] For a homogeneous single TE material, the maximum efficiency will be attained by considering the Thomson heat, and then a CTD model of $\sigma$, $\kappa$, and $S$, expressed as:[69,70]

$$\eta_{max} = \eta_c \frac{\sqrt{1+(ZT)_{eng}(\hat{\alpha}/\eta_c - 1/2)}-1}{\left(\hat{\alpha}\sqrt{1+(ZT)_{eng}(\hat{\alpha}/\eta_c - 1/2)}+1\right)-\eta_c} \quad (5)$$

where $\eta_c$ represents Carnot efficiency given as $\eta_c = (T_H - T_C)/T_H$ and $\hat{\alpha}$ represents the intensity factor of the Thomson effect. Using the CTD model, the predicted maximum efficiency was obtained ($\eta \sim 8\%$) for higher wheel speed (31 m/s), as shown in Fig. 4d. The efficiency calculated by the CPM is twice the efficiency estimated by the CTD model. The $ZT$ was found to be maximum for higher wheel speed (31 m/s), as shown in Fig. 4e. An enhanced $ZT \sim 0.94$ at 1123 K in $p$-type $Si_{80}Ge_{20}$ nano-alloys was obtained by employing MS-SPS at maximum wheel speed (31 m/s). The enhanced $ZT$ corresponds to $\approx$ 88% enhancement in $ZT$ when compared with currently used RTGs[2] in deep space flight missions, and $\approx$ 45% higher than pressure-sintered $p$-type alloys.[10,11,16] Figure 4f shows the comparison of $ZT$ values reported in the literature[12] with those in the current study, which validates the effectiveness of the MS-SPS route as a prospective methodology for attaining higher $ZT$ in SiGe alloys. The CTD model leads to a reliable prediction of TE efficiency and output power from materials to the device as compared with the conventional CPM. However, factors such as measurement techniques, contact resistance, coefficient of thermal expansion, and system environment affect the real modules, wherein major efforts have been directed towards minimizing contact resistance.

## Mechanical Properties

The mechanical properties of the TE materials also play an essential role, especially for high-temperature applications. The hardness of the synthesized $p$-type SiGe nanostructured alloys was measured employing the Vickers microhardness test. The measured hardness values were found to be approximately 3.67, 6.35, and 4.99 GPa for the samples synthesized at 23 m/s, 27 m/s, and 31 m/s, respectively, which is significantly higher than other well-reported TE materials.[3,72] This suggests that the rapid solidification process not only enhanced the TE performance but also substantially improved the microhardness, which is a prerequisite for the durability of TEGs.

## CONCLUSION

In summary, the advantage of rapid solidification coupled with SPS has been realized for attaining a maximum $ZT \sim 0.94$ at 1123 K in $p$-type $Si_{80}Ge_{20}$ nano-alloys, which corresponds to $\approx$ 88% enhancement over its bulk counterpart which is currently being used in deep space explorations, and $\approx$ 45% higher than pressure-sintered $p$-type alloys of similar composition. Moreover, the observed increase in the $ZT$ at high temperature may be ascribed to a synergistic increase in PF and $\kappa$ reduction, owing to multi-scale microstructural features comprising nano-crystallites and a high density of defects in the rapidly solidified MS-SPS samples, which also exhibited higher $P_d$ and $ZT_{eng}$ resulting in $\eta_{max} \approx$

8% as calculated for measured TE transport using the CTD model, thus making them ideal candidates for high-temperature TE applications. Moreover, all MS-SPS samples exhibited hardness in the range of 3.67–6.35 GPa, which is significantly higher than other high-temperature TE materials.[72] Thus, the MS-SPS technique provides an effective paradigm for the optimization of TE properties and can be readily explored in similar TE materials for attaining high TE performance.

## ACKNOWLEDGMENTS

The authors sincerely acknowledge the Director of CSIR-NPL for providing facilities and financial support by BRNS (Board of Research in Nuclear Sciences), Department of Atomic Energy, and Sanction No: 37(3)/14/22/2016-BRNS India, respectively. The corresponding author (Dr. Sivaiah Bathula) sincerely acknowledges the Indian Institute of Technology (IIT) Bhubaneswar (Sanction No: SP095) for financial support. Mr. Avinash Vishwakarma acknowledges DST-INSPIRE SRF, India, for financial support. KKJ and RB are sincerely acknowledges CSIR-India, DST-India, respectively, for providing the financial support. The authors acknowledge the services rendered by Mr. Radhey Shyam and Mr. Naval Kishor Upadhyay. This manuscript was checked for plagiarism by Turnitin software.

## DATA AVAILABILITY

The data that support the findings of this study is available upon request from the authors.

## CONFLICT OF INTEREST

The authors declare that they have no conflict of interest.

## REFERENCES

1. R. O'Brien, R. Ambrosi, N. Bannister, S. Howe, and H.V. Atkinson, *J. Nucl. Mater.* 377, 506–521 (2008).
2. D.M. Rowe, *CRC Handbook of Thermoelectrics* (Boca Raton: CRC Press, 1995).
3. S. Bathula, M. Jayasimhadri, B. Gahtori, N.K. Singh, K. Tyagi, A. Srivastava, and A. Dhar, *Nanoscale* 7, 12474–12483 (2015).
4. N.S. Chauhan, S. Bathula, B. Gahtori, Y.V. Kolen'ko, R. Shyam, N. Upadhyay, and A. Dhar, *J. Appl. Phys.* 126, 125110 (2019).
5. R. Bhardwaj, A. Bhattacharya, K. Tyagi, B. Gahtori, N.S. Chauhan, A. Vishwakarma, K.K. Johari, S. Bathula, S. Auluck, and A. Dhar, *Intermetallics* 112, 106541 (2019).
6. N.S. Chauhan, S. Bathula, A. Vishwakarma, R. Bhardwaj, K.K. Johari, B. Gahtori, and A. Dhar, *Mater. Lett.* 228, 250–253 (2018).
7. R. Bhardwaj, B. Gahtori, K.K. Johari, S. Bathula, N.S. Chauhan, A. Vishwakarma, S. Dhakate, S. Auluck, and A. Dhar, *ACS Appl. Energy Mater.* 2, 1067–1076 (2019).
8. A. Usenko, D. Moskovskikh, M. Gorshenkov, A. Korotitskiy, S. Kaloshkin, A. Voronin, and V. Khovaylo, *Scr. Mater.* 96, 9–12 (2015).
9. M.G. Kanatzidis, *Chem. Mater.* 22, 648–659 (2010).
10. D. Rowe, V. Shukla, and N. Savvides, *Nature* 290, 765–766 (1981).
11. J. Dismukes, L. Ekstrom, E. Steigmeier, I. Kudman, and D. Beers, *J. Appl. Phys.* 35, 2899–2907 (1964).
12. G. Joshi, H. Lee, Y. Lan, X. Wang, G. Zhu, D. Wang, R.W. Gould, D.C. Cuff, M.Y. Tang, and M.S. Dresselhaus, *Nano Lett.* 8, 4670–4674 (2008).
13. S. Bathula, M. Jayasimhadri, N. Singh, A. Srivastava, J. Pulikkotil, A. Dhar, and R. Budhani, *Appl. Phys. Lett.* 101, 213902 (2012).
14. W. Xie, X. Tang, Y. Yan, Q. Zhang, and T.M. Tritt, *Appl. Phys. Lett.* 94, 102111 (2009).
15. Y. Zheng, H. Xie, Q. Zhang, A. Suwardi, X. Cheng, Y. Zhang, W. Shu, X. Wan, Z. Yang, and Z. Liu, *ACS Appl. Mater. Interfaces.* 12, 36186–36195 (2020).
16. E. Koukharenko, N. Frety, V. Shepelevich, and J. Tedenac, *J. Alloys Compd.* 299, 254–257 (2000).
17. Y. Horio, H. Yamashita, and T. Hayashi, *Mater. Trans.* 45, 2757–2760 (2004).
18. W. Xie, S. Wang, S. Zhu, J. He, X. Tang, Q. Zhang, and T.M. Tritt, *J. Mater. Sci.* 48, 2745–2760 (2013).
19. X. Cai, Z. Rong, F. Yang, Z. Gan, and G. Li, *J. Phys. D Appl. Phys.* 47, 115101 (2014).
20. V. Ohorodniichuk, A. Dauscher, E. Branco Lopes, S. Migot, C. Candolfi, and B. Lenoir, *Crystals* 7, 172 (2017).
21. M. Kim, S.-I. Kim, H.-J. Cho, H. Mun, H.-S. Kim, J.-H. Lim, S.W. Kim, and K.H. Lee, *Scr. Mater.* 167, 120–125 (2019).
22. D. Ibrahim, V. Ohorodniichuk, C. Candolfi, C. Semprimoschnig, A. Dauscher, and B. Lenoir, *ACS Omega* 2, 7106–7111 (2017).
23. B. Yang, S. Li, X. Li, Z. Liu, H. Zhong, S. Feng, *J. Alloys Compd.* 155568 (2020).
24. H. Tan, L. Guo, G. Wang, H. Wu, X. Shen, B. Zhang, X. Lu, G. Wang, X. Zhang, and X. Zhou, *ACS Appl. Mater. Interfaces* 11, 23337–23345 (2019).
25. B. Yang, S. Li, X. Li, S. Feng, Z. Liu, and H. Zhong, *J. Mater. Sci.: Mater. Electron.* 29, 18949–18956 (2018).
26. G. Tan, W. Liu, S. Wang, Y. Yan, H. Li, X. Tang, and C. Uher, *J. Mater. Chem. A* 1, 12657–12668 (2013).
27. S. Zhang, X. Zhang, Q. Lu, P. He, T. Lin, and H. Geng, *Mater. Lett.* 260, 126960 (2020).
28. H. Geng, J. Zhang, T. He, L. Zhang, and J. Feng, *Materials* 13, 984 (2020).
29. K.H. Lee, S.H. Bae, and S.-M. Choi, *Materials* 13, 87 (2020).
30. K.W. Bae, J.Y. Hwang, S.-I. Kim, H.M. Jeong, S. Kim, J.-H. Lim, H.-S. Kim, and K.H. Lee, *Appl. Sci.* 10, 4963 (2020).
31. C. Yu, T.-J. Zhu, K. Xiao, J. Jin, J.-J. Shen, S.-H. Yang, and X.-B. Zhao, *J. Inorg. Mater.* 25, 569–572 (2010).
32. C. Yu, T. Zhu, K. Xiao, J. Shen, and X. Zhao, *Funct. Mater. Lett.* 3, 227–231 (2010).
33. J. Xie, Y. Ohishi, S. Ichikawa, H. Muta, K. Kurosaki, and S. Yamanaka, *J. Appl. Phys.* 121, 205107 (2017).
34. S. Muthiah, R. Singh, B. Pathak, P.K. Avasthi, R. Kumar, A. Kumar, A. Srivastava, and A. Dhar, *Nanoscale* 10, 1970–1977 (2018).
35. X. Tang, G. Wang, Y. Zheng, Y. Zhang, K. Peng, L. Guo, S. Wang, M. Zeng, J. Dai, and G. Wang, *Scr. Mater.* 115, 52–56 (2016).
36. D. Souda, K. Shimizu, Y. Ohishi, H. Muta, T. Yagi, and K. Kurosaki, *ACS Appl. Energy Mater.* 3, 1962–1968 (2020).
37. D. Qi, X. Tang, H. Li, Y. Yan, and Q. Zhang, *J. Electron. Mater.* 39, 1159–1165 (2010).
38. B. Du, H. Li, J. Xu, X. Tang, and C. Uher, *J. Solid State Chem.* 184, 109–114 (2011).
39. H. Tan, B. Zhang, G. Wang, Y. Chen, X. Shen, L. Guo, X. Han, X. Lu, and X. Zhou, *J. Alloys Compd.* 774, 129–136 (2019).
40. E. Nshimyimana, X. Su, H. Xie, W. Liu, R. Deng, T. Luo, Y. Yan, and X. Tang, *Sci. Bull.* 63, 717–725 (2018).
41. F. Alshmri, *Advanced Materials Research, Trans Tech Publ,* 1740–1746 (2012).
42. S. Wongprakarn, S. Pinitsoontorn, S.-A. Tanusilp, and K. Kurosaki, *Mater. Sci. Semicond. Process.* 88, 239–249 (2018).
43. N.S. Chauhan, S. Bathula, A. Vishwakarma, R. Bhardwaj, K.K. Johari, B. Gahtori, M. Saravanan, and A. Dhar, *J. Phys. Chem. Solids* 123, 105–112 (2018).

44. P. Ramachandrarao, *Bull. Mater. Sci.* 15, 503–513 (1992).
45. J. Sun, Z. Zhang, C. Cui, W. Yang, P. Guo, D. Han, and B. Wang, *J. Alloys Compd.* 476, 575–578 (2009).
46. W. Cai, Y. Feng, J. Sui, Z. Gao, and G. Dong, *Scr. Mater.* 58, 830–833 (2008).
47. J. Zhang, T. Ma, and M. Yan, *Phys. B* 404, 4155–4158 (2009).
48. L. Han, S.H. Spangsdorf, N. Nong, L. Hung, Y. Zhang, H.N. Pham, Y. Chen, A. Roch, L. Stepien, and N. Pryds, *RSC Adv.* 6, 59565–59573 (2016).
49. S. Liu, C. Cui, X. Wang, N. Li, J. Shi, S. Cui, and P. Chen, *Metals* 7, 204 (2017).
50. N. Gaur, C. Bhandari, and G. Verma, *Phys. Rev.* 144, 628 (1966).
51. M.L. Snedaker, Y. Zhang, C.S. Birkel, H. Wang, T. Day, Y. Shi, X. Ji, S. Kraemer, C.E. Mills, and A. Moosazadeh, *Chem. Mater.* 25, 4867–4873 (2013).
52. Z. Zamanipour, X. Shi, A.M. Dehkordi, J.S. Krasinski, and D. Vashaee, *Phys. Status Solidi (a)* 209, 2049–2058 (2012).
53. Z. Zamanipour, J.S. Krasinski, and D. Vashaee, *J. Appl. Phys.* 113, 143715 (2013).
54. G.J. Snyder, E.S. Toberer, *World Scientific* 101–110 (2011).
55. T. Zhu, H. Gao, Y. Chen, and X. Zhao, *J. Mater. Chem. A* 2, 3251–3256 (2014).
56. H.-S. Kim, Z.M. Gibbs, Y. Tang, H. Wang, and G.J. Snyder, *APL Mater.* 3, 041506 (2015).
57. B. Madavali and S.-J. Hong, *J. Electron. Mater.* 45, 6059–6066 (2016).
58. Y. Tang, X. Li, L.H. Martin, E.C. Reyes, T. Ivas, C. Leinenbach, S. Anand, M. Peters, G.J. Snyder, and C. Battaglia, *Energy Environ. Sci.* 11, 311–320 (2018).
59. J. Nie, R. Ranganathan, Z. Liang, and P. Keblinski, *J. Appl. Phys.* 122, 045104 (2017).
60. D. Rowe and N. Savvides, *J. Phys. D Appl. Phys.* 12, 1613 (1979).
61. G.J. Snyder and T.S. Ursell, *Phys. Rev. Lett.* 91, 148301 (2003).
62. N.S. Chauhan, A. Bhardwaj, T. Senguttuvan, R. Pant, R. Mallik, and D. Misra, *J. Mater. Chem. C* 4, 5766–5778 (2016).
63. G.J. Snyder, *Appl. Phys. Lett.* 84, 2436–2438 (2004).
64. N.S. Chauhan, S. Bathula, A. Vishwakarma, R. Bhardwaj, K.K. Johari, B. Gahtori, and A. Dhar, *J. Materiom.* 5, 94–102 (2019).
65. N.K. Upadhyay, N.S. Chauhan, L. Kumaraswamidhas, K.K. Johari, B. Gahtori, S. Bathula, R. Reddy, Y.V. Kolen'ko, S.R. Dhakate, and A. Dhar, *Mater. Lett.* 265, 127428 (2020).
66. N.K. Upadhyay, L. Kumaraswamidhas, B. Gahtori, S. Bathula, S. Muthiah, R. Shyam, N.S. Chauhan, R. Bhardwaj, and A. Dhar, *J. Alloys Compd.* 765, 412–417 (2018).
67. N.S. Chauhan, S. Bathula, B. Gahtori, Y.V. Kolen'ko, and A. Dhar, *J. Electron. Mater.* 48, 6700–6709 (2019).
68. R. He, D. Kraemer, J. Mao, L. Zeng, Q. Jie, Y. Lan, C. Li, J. Shuai, H.S. Kim, and Y. Liu, *Proc. Natl. Acad. Sci.* 113, 13576–13581 (2016).
69. H.S. Kim, W. Liu, G. Chen, C.-W. Chu, and Z. Ren, *Proc. Natl. Acad. Sci.* 112, 8205–8210 (2015).
70. H.S. Kim, W. Liu, and Z. Ren, *Energy Environ. Sci.* 10, 69–85 (2017).
71. H. Armstrong, M. Boese, C. Carmichael, H. Dimich, D. Seay, N. Sheppard, and M. Beekman, *J. Electron. Mater.* 46, 6–13 (2017).
72. G. Schierning, R. Chavez, R. Schmechel, B. Balke, G. Rogl, and P. Rogl, *Transl. Mater. Res.* 2, 025001 (2015).